ACS OMEGA

http://pubs.acs.org/journal/acsodf

Article

One-Pot Synthesis of High-Performance Tin Chalcogenides/C Anodes for Li-Ion Batteries

Xianyu Liu, Tayyaba Najam, Ghulam Yasin, Mohan Kumar, and Miao Wang*

Cite This: *ACS Omega* 2021, 6, 17391−17399

Read Online

ACCESS | Metrics & More | Article Recommendations | Supporting Information

ABSTRACT: Tin chalcogenides are considered as promising anode materials for lithium-ion batteries (LIBs) due to their high theoretical lithium-storage capacity. Herein, we have successfully synthesized the composites of tin chalcogenides and graphite, that is, SnS/C, SnSe/C, and $SnS_{0.5}Se_{0.5}$/C, via a simple one-pot solid-state method. During the electrochemical test, they exhibit excellent lithium-storage ability and cyclic performance as the anode electrodes of LIBs due to the introduction of carbon. In particular, (i) SnS/C displayed a high specific capacity of 875 mAh g^{-1} at 0.2 A g^{-1} over 200 cycles; (ii) SnSe/C presents 734 mAh g^{-1} at 0.2 A g^{-1} after 100 cycles, and it delivers 690 mAh g^{-1} at 1.0 A g^{-1} over 300 cycles; and (iii) the $SnS_{0.5}Se_{0.5}$/C composite electrode delivers a specific capacity of 643 mAh g^{-1} at 0.5 A g^{-1} over 150 cycles. Furthermore, another series of tin-based composites have also been successfully fabricated (i.e., Sn/C, SnS_2/C, $SnSe_2$/C, and SnTe/C), showing the general applicability of the synthetic route applied here. Our synthetic approach demonstrates a promising route for the large-scale production of high-performance tin chalcogenides/C anode materials for LIBs and other battery systems (e.g., Na-ion and K-ion batteries).

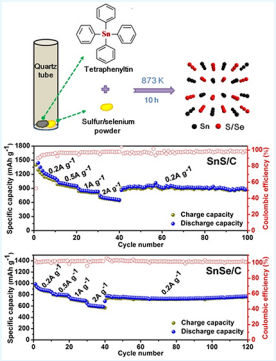

INTRODUCTION

Due to the shortage of fossil energy and the environmental pollution caused by fossil energy, electric vehicles powered by lithium-ion batteries (LIBs) are more and more popular in the auto market.[1−3] However, facing the competition of internal combustion engines, there is an urgent demand for the improvement of energy densities of LIBs. Nowadays, the widely used anode material of LIBs is graphite, owing to its low cost and high chemical stability. However, the theoretical specific capacity of graphite is relatively low, only 372 mAh g^{-1}.[4−7] Thus, massive research works have been done to develop alternative anodes with enhanced specific capacities.[8−10] Tin-based compounds such as tin metal,[11,12] tin oxides,[13,14] tin chalcogenides,[15,16] and tin phosphides[17,18] have been considered as a promising family for alternative anodes owing to their high theoretical specific capacity, cost-effectiveness, and eco-friendliness. However, these materials have huge volume change problems during the charging/discharging cycling, causing poor stability. Over the last decade, a lot of efforts have been dedicated to solve these problems. These efforts can be generally categorized into two types: (i) decreasing the particle size into nanoscale to protect the structural integrity and (ii) combining tin-based compounds with conductive materials (e.g., graphite) to alleviate volume expansion and particle aggregation.[19−23] Based on these efforts, a large number of literature about carbon-modified tin or tin chalcogenides, for example, Sn/C,[24,25] SnS/C,[26,27] and SnSe/C,[28,29] had been reported and they exhibited improved electrochemical properties for Li-ion batteries.

Up to now, the reported pathways for the synthesis of tin chalcogenides mainly include the solvothermal method,[26,28] hydrothermal method,[30] solution method,[31] coprecipitation method,[32] and chemical vapor transport.[33] However, these synthetic approaches have shown several drawbacks at present, such as complicated reaction conditions and relatively poor repeatability. Herein, we developed a simple one-pot route by employing tetraphenyltin as the tin source and successfully synthesized Sn(S, Se)/C composites without any complex equipment, harsh reagents, and reaction conditions. Elemental analysis revealed that the carbon contents of the as-synthesized SnS/C, SnSe/C, and $SnS_{0.5}Se_{0.5}$/C were 32.8, 31.6, and 36.8 wt %, respectively. During the electrochemical test, the as-synthesized Sn(S, Se)/C composites exhibited excellent electrochemical properties, which were comparable to the best properties of Sn(S, Se) anode materials reported in the literature. Furthermore, we extended the one-pot route to synthesize other series of tin-based composites, demonstrating the general applicability for the synthesis of high-performance tin-based anode materials.

EXPERIMENTAL SECTION

Materials. Tetraphenyltin ($Sn(C_6H_5)_4$, 97% purity), sublimate sulfur (99.95% purity), selenium powder (99.9% purity), tellurium powder (99.9% purity), dibenzyl disulfide

Received: March 27, 2021
Accepted: June 21, 2021
Published: June 30, 2021

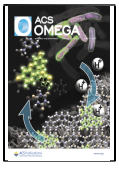

(98% purity), and dibenzyl diselenide (95% purity) were purchased from Aladdin Company. No further purification of reagents was done.

Synthetic Methods. For the typical synthesis of SnS/C and SnSe/C composites, powders of 0.2 g of tetraphenyltin and 0.015 g of sublimate sulfur or 0.037 g of selenium powder were mixed together and sealed in a vacuumized quartz tube. Then, the quartz tube was annealed at 873 K for 10 h. The $SnS_{0.5}Se_{0.5}$/C composite was prepared from a stoichiometric mixture of tetraphenyltin, sublimate sulfur, and selenium powder. The mixture was then sealed in a vacuumized quartz tube and annealed at 873 K for 10 h. Scheme 1 schematically illustrates the synthetic process for Sn(S,Se)/C composites. Then, the as-prepared product was collected, washed several times with DI water and absolute alcohol, and dried in a vacuum oven at 60 °C.

Scheme 1. Schematic Illustration of Synthetic Routes for Sn(S,Se)/C Composites

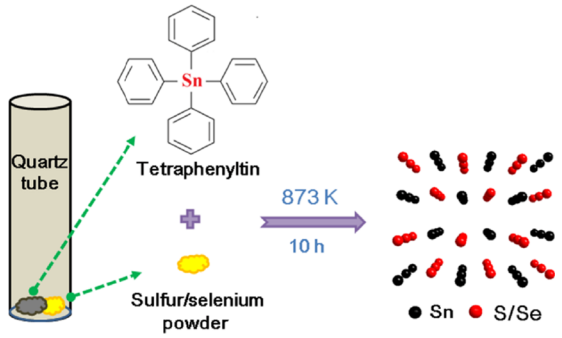

Structural Characterization. The purity of the samples was examined by powder XRD on a Philips X'Pert diffractometer with a Cu Kα radiation (λ = 1.5418 Å). Field emission scanning electron microscopy (SEM, JEOLJSM-6700F) was used for the morphological studies of the prepared samples. X-ray photoelectron spectral studies were performed on Thermo ESCALAB 250. All spectra were calibrated by the C 1s peak resulting from the graphite. The stoichiometric ratios of tin chalcogenides were derived from the XPS data. TGA measurements were performed in an air environment from room temperature (RT) to 800 °C with a heating rate of 10 °C min^{-1}. Raman spectroscopy was performed on a JY LABRAM-HR confocal laser micro-Raman spectrometer utilizing Ar^+ laser excitation (λ = 514.5 nm). The carbon content was examined by elemental analysis (EA, Elemental vario EL cube, Thermal Conductivity Detector) under an oxygen atmosphere. Energy-dispersive spectrometer (EDS) images were taken at an acceleration voltage of 200 kV (JEOL-2010 HRTEM).

Electrochemical Characterization. An argon-filled glovebox (O_2, H_2O < 1 ppm) enclosing a counter electrode (lithium foil), a separator (Celgard 2400), and 1.0 M $LiPF_6$ in ethylene carbonate (EC)/diethyl carbonate (DEC) in the volume ratio of 1:1 as the electrolyte was used to keep assembled coin-type 2016 cells. For the preparation of the working electrode, active material, polyvinylidene fluoride (PVDF), and carbon black at a weight ratio of 6:2:2 were mixed in *N*-methyl-2-pyrrolidone. The found mixture was ball-milled (10 h) to mix uniformly, and the obtained slurry was spread on the substrate (Cu foil) and dried (80 °C) in a vacuum oven (10 h). Cyclic voltammetric (CV) experiments were conducted at a scan rate of 0.1 mV s^{-1} (electrochemical workstation, CHI660E). Galvanostatic measurements were examined using a LAND-CT2001A instrument in the potential range of 0.01−3 V (vs Li/Li^+) at a selected current density and constant RT. Here, the specific capacities and currents were calculated based on the total mass of the anode materials.

RESULTS AND DISCUSSION

The phases of the as-prepared samples are examined by powder XRD, and the results are displayed in Figures 1a and 2a: orthorhombic SnS/C (JCPDS card no. 39-0354, *Pmcn*, *a* = 3.98 Å, *b* = 4.33 Å, *c* = 11.18 Å) and orthorhombic SnSe/C (JCPDS card no. 65-3811, *Pnma*, *a* = 11.59 Å, *b* = 4.21 Å, *c* = 4.41 Å), respectively. The morphologies and microstructures of the as-synthesized products are characterized by SEM, TEM, high-resolution TEM (HRTEM), high-angle annular dark-field STEM (HAADF-STEM), and EDX mapping. Figures 1b and S1 are the SEM images of the as-prepared SnS/C sample, revealing the uneven aggregation of particles. For the

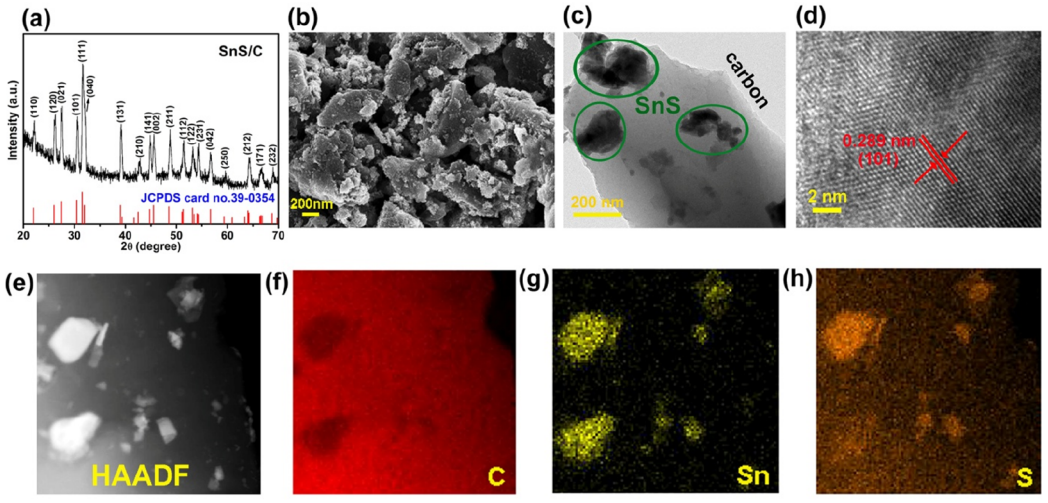

Figure 1. (a) Powder XRD pattern of the SnS/C sample. (b) SEM, (c) TEM, and (d) HRTEM images of the SnS/C sample. (e−h) HAADF-STEM and corresponding EDX images of the SnS/C sample.

https://doi.org/10.1021/acsomega.1c01647
ACS Omega 2021, 6, 17391−17399

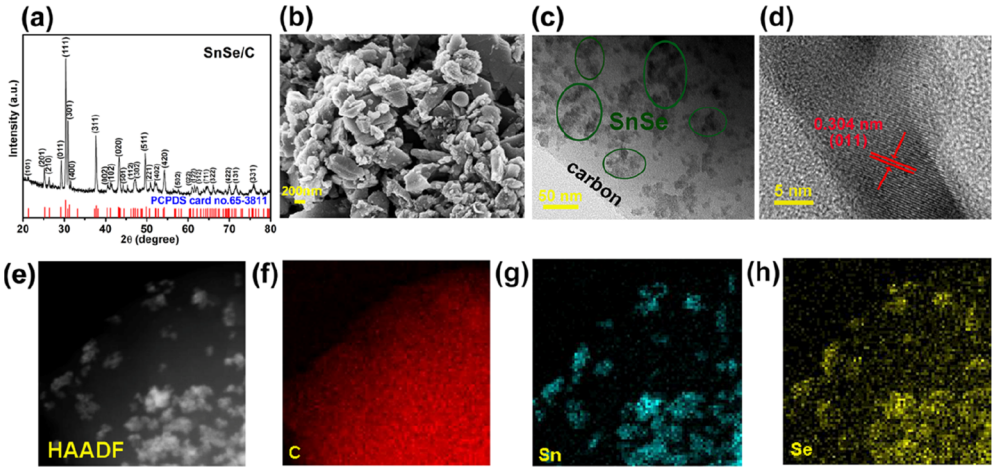

Figure 2. (a) Powder XRD pattern of the SnSe/C sample. (b) SEM, (c) TEM, and (d) HRTEM images of the SnSe/C sample. (e–h) HAADF-STEM and the corresponding EDX images of the SnSe/C sample.

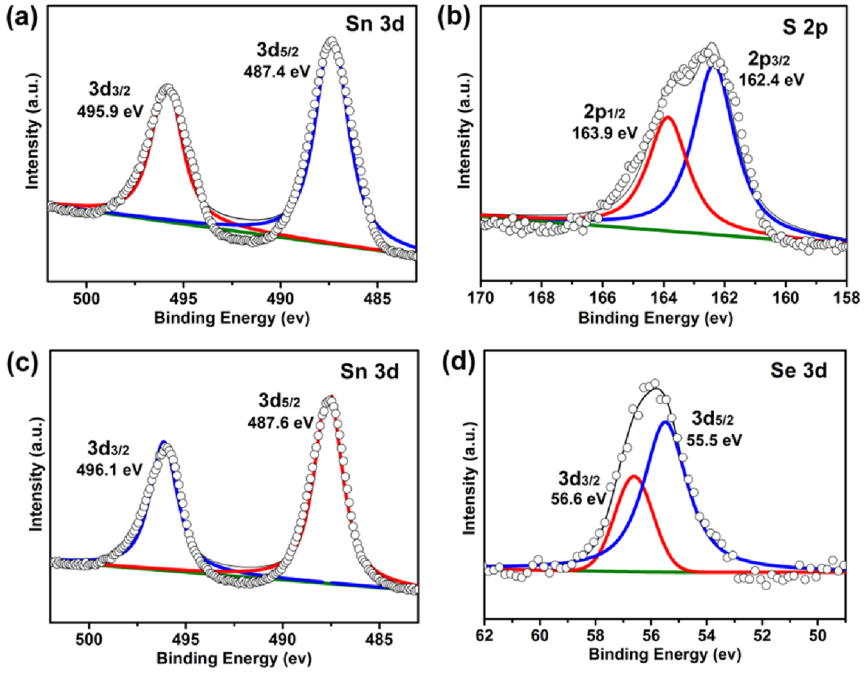

Figure 3. XPS for (a) Sn 3d and (b) S 2p levels of the SnS/C sample. XPS for (c) Sn 3d and (d) Se 3d levels of the SnSe/C sample.

identification of the microstructure of the SnS/C sample, TEM characterization was conducted with the results shown in Figure 1c–h. In Figure 1c, the TEM image demonstrates the combination of SnS nanoparticles and carbon layers and the irregular morphology of the SnS nanoparticles marked with green circles. Figure 1d shows the HRTEM image of the SnS/C sample, and the selected lattice fringe is about 0.289 nm wide, which corresponds to the *d*-spacing of the (101) plane of SnS. The HAADF-STEM image in Figure 1e and the corresponding EDX images in Figure 1f–h further confirmed the distribution of SnS nanoparticles on carbon layers and the compositional elements (i.e., Sn, S, and C) of the SnS/C sample. The EDX (Figure S4) indicates that this composite is composed of C, Sn, and S elements and the signal of Cu arises from the TEM grid.

From the SEM images in Figures 2b and S2, it could be found that the SnSe/C sample shows an unfixed lumpy morphology similar to that of the SnS/C sample. The TEM images in Figures 2c and S3 reveal that the diameter of the SnSe nanoparticles is around a few to tens of nanometers and the SnSe nanoparticles disperse over the carbon layer without severe agglomeration. The lattice fringe in the HRTEM image (Figure 2d) of the SnSe/C sample is about 0.304 nm wide, which matches the *d*-spacing of the (011) plane of SnSe. Similar to the SnS/C sample, the HAADF-STEM image in Figure 2e and the corresponding EDX images in Figure 2f–h further confirmed the distribution of SnSe nanoparticles on carbon layers and the compositional elements (i.e., Sn, Se, and C) of the SnSe/C sample. The EDX spectra in Figure S5 shows that the SnSe/C composite is composed of C, Sn, and Se elements and note that the trace oxygen signal may be caused by slight surface oxidation.

The images in Figure 3 reveal the XPS characterization results of the SnS/C and SnSe/C samples. In Figure 3a, the two peaks at around 487.4 and 495.9 eV correspond to Sn $3d_{5/2}$ and $3d_{3/2}$, respectively.[34,35] The S $2p_{3/2}$ at 162.4 eV and S

https://doi.org/10.1021/acsomega.1c01647
ACS Omega 2021, 6, 17391−17399

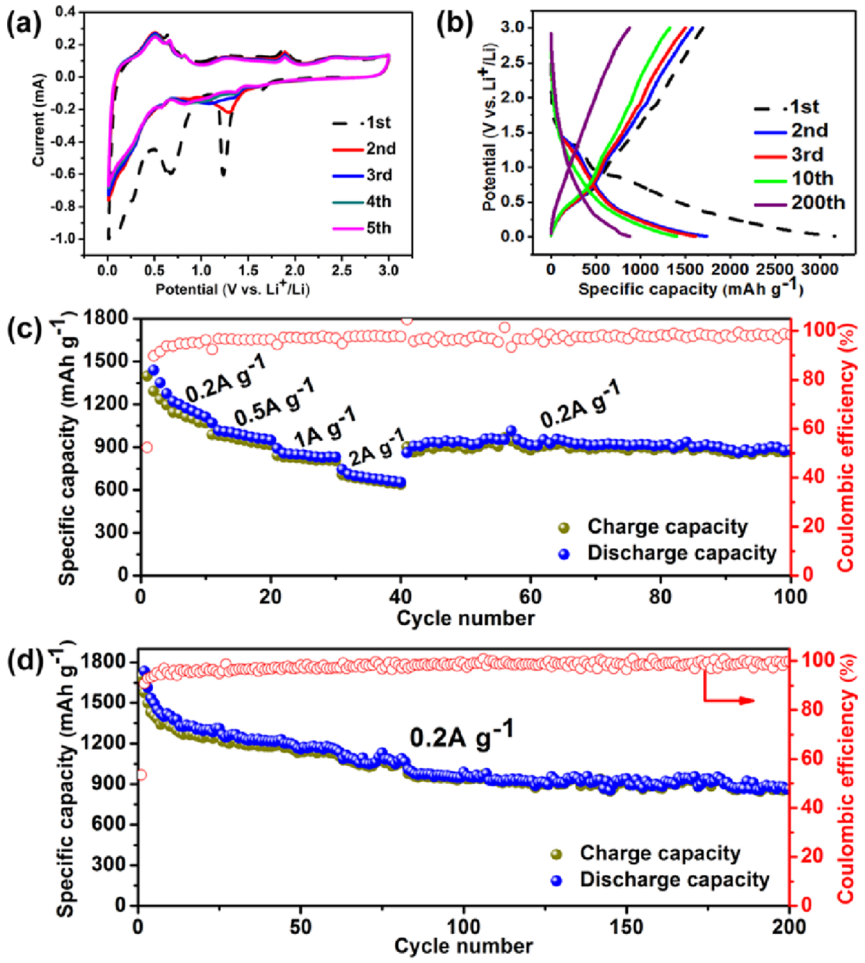

Figure 4. (a) CV curves of the SnS/C sample. (b) Galvanostatic charging−discharging curves of the SnS/C sample at 0.2 A g^{-1}. (c) Rate capability of the SnS/C sample from 0.2 to 2.0 A g^{-1}. (d) Cycling performance and Coulombic efficiency (CE) of the SnS/C sample at 0.2 A g^{-1}.

$2p_{1/2}$ at 163.9 eV shown in Figure 3b are ascribed to the binding energies of SnS, which suggests that no elemental sulfur (165.1 eV in binding energy) remains in the composite.[36,37] The C 1s peak at 284.7 eV corresponding to the C−C bonding in carbon is displayed in Figure S6.[38] The peaks at 487.6 and 496.1 eV in Figure 3c can be related to Sn $3d_{5/2}$ and $3d_{3/2}$ of SnSe.[34,35] As shown in Figure 3d, the peaks at 55.5 and 56.6 eV denote the spin−orbit splitting of $3d_{5/2}$ and $3d_{3/2}$ of Se.[39] The peak at 284.8 eV corresponds to the C 1s peak (Figure S7).[38]

For electrochemical tests, CV was first utilized to understand the dynamic process of the SnS/C sample for lithiation/delithiation. Figure 4a reveals the CV curves of the first five cycles of the SnS/C sample. From the negative scanning curve of the first cycle, two reduction peaks located at 1.24 V could be detected, which are in connection with the irreversible decomposition of SnS into Sn and Li_2S (1).[30] The reduction peak at 0.75 V is related to the reactions between the electrode materials and the electrolyte, which cause the formation of the SEI membrane.[9,10] The reduction peak at 0.2 V represents the Li-ion alloying with Sn (2).[31,40]

$$SnS + 2Li^+ + 2e^- \rightarrow Sn + Li_2S \quad (1)$$

$$Sn + xLi \rightarrow Li_xSn \quad (2)$$

In the positive scanning curve of the first cycle, the two broad oxidation peaks at 0.51 and 0.65 V are in relation with the delithiation process of Li_xSn. The oxidation peaks located at 1.87 V originated from the reversible conversion reaction of SnS.

The charging−discharging curves for the 1st, 2nd, 3rd, 10th, and 200th cycles at a current density of 0.2 A g^{-1} of the SnS/C sample are presented in Figure 4b. Consistent with the CV, an obvious platform around 1.3 V can be observed in the initial discharging process. Note that in the subsequent cycles, the platform around 1.3 V gradually weakens due to the irreversible decomposition of SnS. During the charging process, the platform located at around 0.55 V is ascribed to the extraction of Li ions from the discharged SnS/C sample. The charging−discharging curves in Figure 4c exhibit the excellent rate performance of the SnS/C sample. The specific capacities at the currents of 0.2, 0.5, 1.0, and 2.0 A g^{-1} are found to be 1076, 958, 837, and 661 mAh g^{-1}, respectively, and after charging/discharging at high current densities, the specific capacity can recover to 886 mAh g^{-1} at 0.2 A g^{-1}. Figure 4d displays the excellent cyclic performance of the SnS/C sample at 0.2 A g^{-1}. In the first cycle, the specific capacities are found to be 3164 and 1693 mAh g^{-1} during the discharging/charging process, respectively, suggesting an initial Coulombic efficiency (CE) of 53.5% due to the irreversible decomposition of SnS. Then, the CE of the SnS/C sample increases to 98% and remains almost unchanged during the subsequent cycles. After cycling 200 times at 0.2 A g^{-1}, the specific capacity of the SnS/C sample can still remain around

https://doi.org/10.1021/acsomega.1c01647
ACS Omega 2021, 6, 17391−17399

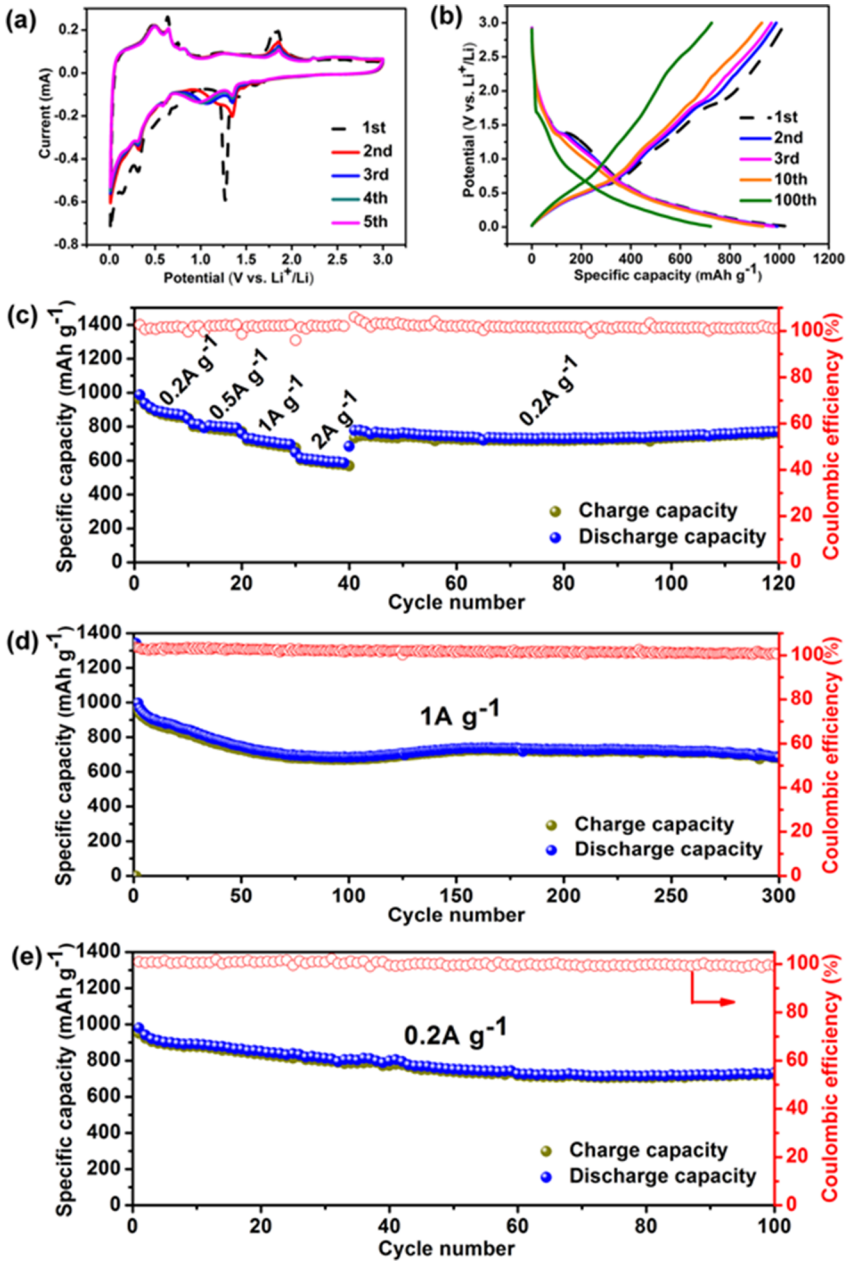

Figure 5. (a) CV curves of the SnSe/C sample. (b) Galvanostatic charging−discharging curves of the SnSe/C sample at 0.2 A g^{-1}. (c) Rate capability of the SnSe/C sample from 0.2 to 2.0 A g^{-1}. (d) Cycling performance and Coulombic efficiency (CE) of the SnSe/C sample at 1.0 A g^{-1}. (e) Cycling performance and CE of the SnSe/C sample at 0.2 A g^{-1}.

875 mAh g^{-1}. Since the specific capacity of graphite is lower than that of SnS, the specific capacity of bare SnS should be higher than the value of the SnS/C sample obtained here. Considering the theoretical specific capacity (i.e., 372 mAh g^{-1}) of graphite and the 32.8 wt % carbon content of the SnS/C sample measured here, the specific capacity of the SnS nanoparticles synthesized through the one-pot route could be roughly estimated to be about 1120 mAh g^{-1} at 0.2 A g^{-1}. The SnS without carbon showed a rapid and continuous capacity attenuation during the electrochemistry cycling process and decreased to 163 mAh g^{-1} after 50th cycles.[33] In comparison to the pure SnS electrode, the SnS/C electrode presented here evidently displays a better Li-storage ability due to the introduction of carbon material.

The electrochemical properties of the SnSe/C sample were measured in the same way as that for the SnS/C sample. Figure 5b presents the 1st, 2nd, 3rd, 10th, and 100th charging−discharging curves of the SnSe/C sample at the current of 0.2 A g^{-1}. It could be observed that the SnSe/C sample also shows a discharging platform observed at 1.4 V in the first charging/discharging cycle, and the platform disappears in the subsequent cycles, which is assigned to the irreversible degradation of SnSe into metallic tin and Li_2Se:[28,29]

$$SnSe + 2Li^+ + 2e^- \rightarrow Sn + Li_2Se \quad (3)$$

During the subsequent charging processes, the two platforms located at 0.5 and 1.8 V originate from the dealloying reaction of Sn with Li (Figure 5a, discussed later). The first CV curve of the SnSe/C sample in Figure 5a was also collected, in which

https://doi.org/10.1021/acsomega.1c01647
ACS Omega 2021, 6, 17391−17399

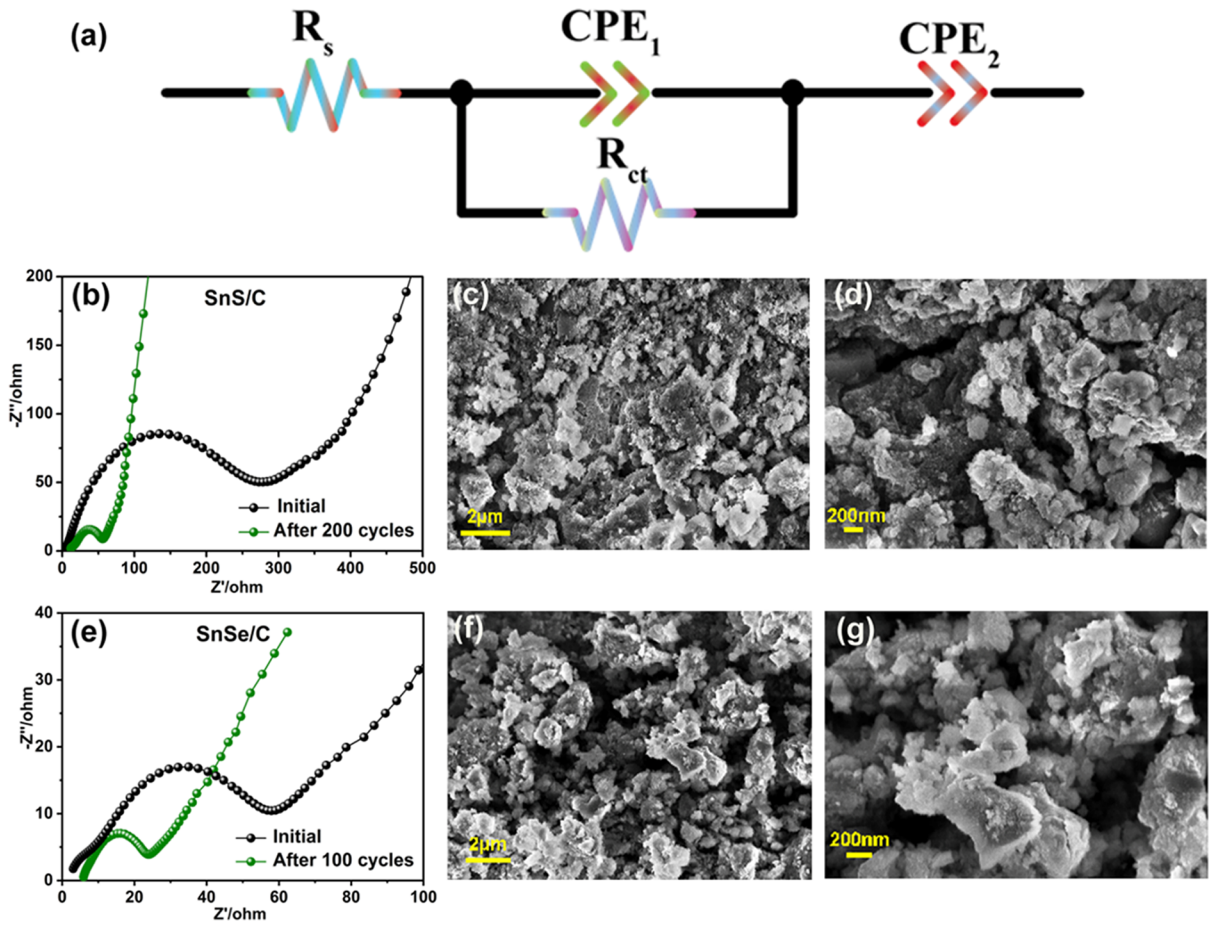

Figure 6. (a) Equivalent circuit model to fit the Nyquist plots. R_s is the contact resistance between the electrode and electrolyte; R_{ct} is charge transfer resistance; and CPE is the constant phase element. (b) EIS of the SnS/C sample before cycling and after 200 cycles at 0.2 A g^{-1}, (c) Low-magnified and (d) high-magnified SEM images of the SnS/C composite electrode after 200 cycles at 0.2 A g^{-1}. (e) EIS of the SnSe/C composite electrode before cycling and after 100 cycles at 0.2 A g^{-1}. (f) Low-magnified and (g) high-magnified SEM images of the SnSe/C composite electrode after 200 cycles at 0.2 A g^{-1}.

the redox peaks are in accordance with the charging–discharging curves in Figure 5b. Obviously, the reduction peak around 0.25 V represents the Li alloying with Sn:[28,29]

$$\mathrm{Sn} + x\mathrm{Li}^+ + x\mathrm{e}^- \rightarrow \mathrm{Li}_x\mathrm{Sn} \quad (4)$$

As for the rate capabilities of the SnSe/C sample, the specific capacities at 0.2, 0.5, 1.0, 2.0, and 0.2 A g^{-1} estimated from Figure 5c are around 861, 789, 702, 593, and 738 mAh g^{-1}, respectively. They only undergo a capacity loss of 31.1% with the current density increasing from 0.2 to 2.0 A g^{-1}, suggesting a relatively good rate capability. Figure 5e displays the cyclic performance of the SnSe/C sample at the current density of 0.2 A g^{-1}. After the first cycle, the SnSe/C sample shows a high specific capacity with the CE nearly 100%, indicating an excellent ability of energy storage. After 100 cycles at 0.2 A g^{-1}, the specific capacity of the SnSe/C sample maintains around 734 mAh g^{-1}. Moreover, the SnSe/C sample displays a specific capacity of nearly 690 mAh g^{-1} over 300 cycles at 1.0 A g^{-1}, as shown in Figure 5d. In the same way, for estimating the specific capacity of the SnS nanoparticles, the specific capacity of the SnSe nanoparticles is estimated to be around 901 mAh g^{-1} at 0.2 A g^{-1} and 837 mAh g^{-1} at 1.0 A g^{-1}. The SnSe without carbon maintained a specific capacity of only 271 mAh g^{-1} at 0.5 A g^{-1} over 100th cycles,[28] indicating that the carbon-modified SnSe/C electrode demonstrated in this work delivers a significantly enhanced cycling property than the pure SnSe electrode.

To obtain further insight into intrinsic electrochemical mechanisms of composite electrodes, electrochemical impedance spectroscopy (EIS) was used to study the conductivity of the SnS/C and SnSe/C samples before and after electrochemical cycling. Figure 6a displays the equivalent circuit model, where R_s is the internal resistance between the electrolyte and electrode and CPE and R_{ct} correspond to the constant phase element and charge transfer resistance, respectively. The Nyquist plots of the two samples are displayed in Figure 6b,e. The semicircle at the medium-frequency region represents the internal resistances in the electrode.[41] We find that SnS/C and SnSe/C electrodes show observable impedance decrease after electrochemical processes compared to impedance values before cycling, demonstrating that two composites retain good electron transport during the cycled process, which may be ascribed to the carbon introduction.[42,43] On the other hand, the ex situ SEM was carried out to study the morphologies of the two samples after cycling. These two composites maintain similar irregular morphologies before and after cycling, which were considered to be advantageous to the cycling stability due to the good electron transport between the carbon and corresponding matrix, as displayed in Figures 6c,d,f,g.[44,45]

https://doi.org/10.1021/acsomega.1c01647
ACS Omega 2021, 6, 17391−17399

As discussed above, SnS/C, SnSe/C, and $SnS_{0.5}Se_{0.5}$/C composites were successfully synthesized via a simple and cost-effective one-pot route and displayed superior electrochemical properties when utilized as anode materials for LIBs due to the hybridizations of carbon. It can be clearly observed from Table 1 and Figure S11 that the as-synthesized SnS/C, SnSe/C, and $SnS_{0.5}Se_{0.5}$/C composites deliver outstanding lithium-storage capabilities exceeding or comparable to those of the Sn(S,Se)-based anode materials that have been reported in the literature, demonstrating the feasibility of the one-pot route developed in this work for the synthesis of high-performance Sn-based anode materials. The structure and electrochemical performances of other tin-based anode materials are presented in Figures S12−S15.

Table 1. Summary of Electrochemical Performance of Sn(S,Se)/C Anodes in This Work and That of the Previously Typical Literature

materials	cycled capacities	cycle number	reference
SnS/C composite	875 mAh g^{-1} at 0.2 A g^{-1}	200	this work
SnSe/C composite	734 mAh g^{-1} at 0.2 A g^{-1}	100	this work
	690 mAh g^{-1} at 1.0 A g^{-1}	300	
$SnS_{0.5}Se_{0.5}$/C composite	643 mAh g^{-1} at 0.5 A g^{-1}	150	this work
SnS@rGO	791 mAh g^{-1} at 0.1 A g^{-1}	100	26
SnS/C hybrid	466 mAh g^{-1} at 0.05 A g^{-1}	50	27
SnS nanoflower	580 mAh g^{-1} at 0.05 A g^{-1}	30	31
SnS/polypyrrole nanosheet	703 mAh g^{-1} at 1.0 A g^{-1}	500	32
SnS nanosheet	560 mAh g^{-1} at 0.78 A g^{-1}	50	33
SnS@polypyrrole-nanobelt/carbon nanotube	757 mAh g^{-1} at 1.0 A g^{-1}	500	46
SnS nanocrystal	867 mAh g^{-1} at 0.1 A g^{-1}	70	47
net-like SnS/C film	540 mAh g^{-1} at 0.04 A g^{-1}	40	48
SnS/C nanofibers	648 mAh g^{-1} at 0.2 A g^{-1}	500	40
	548 mAh g^{-1} at 0.5 A g^{-1}	500	
SnS/C nanosphere	936 mAh g^{-1} at 0.1 A g^{-1}	50	49
	830 mAh g^{-1} at 0.5 A g^{-1}	250	
SnS/TiO_2@C nanosphere	672 mAh g^{-1} at 0.5 A g^{-1}	100	50
NG−SnS composite	790 mAh g^{-1} at 0.5 A g^{-1}	900	51
SnS/C nanocomposite	696 mAh g^{-1} at 0.5 A g^{-1}	200	52
	423 mAh g^{-1} at 2.0 A g^{-1}	200	
SnS/graphene nanosheet	840 mAh g^{-1} at 0.1 A g^{-1}	150	53
YDSC-SnS@NSC	561 mAh g^{-1} at 1.0 A g^{-1}	100	54
	344 mAh g^{-1} at 2.0 A g^{-1}	600	
SnS@C nanoparticle	484 mAh g^{-1} at 0.04 A g^{-1}	40	55
Se-doped SnS/C nanofiber	700 mAh g^{-1} at 0.2 A g^{-1}	100	56
SnS/C nanocomposite	607 mAh g^{-1} at 1.0 A g^{-1}	200	57
SnS/NC nanocomposite	832 mAh g^{-1} at 0.1 A g^{-1}	100	58
SnS/graphene	535 mAh g^{-1} at 0.05 A g^{-1}	50	59
flower-likeC@SnS	594 mAh g^{-1} at 0.5 A g^{-1}	100	60
SnS/spherical grapheme framework	800 mAh g^{-1} at 0.078 A g^{-1}	100	61
	527 mAh g^{-1} at 0.78 A g^{-1}	300	
SnSe/C nanocomposite	633 mAh g^{-1} at 0.5 A g^{-1}	100	28
SnSe@CNF composite	840 mAh g^{-1} at 0.2 A g^{-1}	100	29
SnSe nanocrystal	510 mAh g^{-1} at 0.1 A g^{-1}	70	47
SnSe−MWCNT hybrid	651 mAh g^{-1} at 0.05 A g^{-1}	50	62
SnSe quantum dot	550 mAh g^{-1} at 0.5 A g^{-1}	1500	63
SnSe/C nanofiber	405 mAh g^{-1} at 1.0 A g^{-1}	500	64
$SnS_{0.5}Se_{0.5}$ nanocomposite	625 mAh g^{-1} at 0.5 A g^{-1}	1000	34
$SnS_{0.5}Se_{0.5}$ nanoplate	681 mAh g^{-1} at 0.5 A g^{-1}	200	65

CONCLUSIONS

Tin chalcogenide-based composites, that is, Sn(S, Se)/C, were successfully synthesized by a facile one-pot route. During the electrochemical test, they displayed excellent lithium-storage capabilities, revealing their potential as the anode materials for LIBs. In particular, the SnS/C composite delivers a specific capacity of 875 mAh g^{-1} after 200 cycles at a current density of 0.2 A g^{-1}, the SnSe/C composite electrode delivers a specific capacity of 734 mAh g^{-1} over 100 cycles at 0.2 A g^{-1} and 690 mAh g^{-1} at 1.0 A g^{-1} after 300 cycles, and the $SnS_{0.5}Se_{0.5}$/C composite electrode delivers a capacity of 643 mAh g^{-1} at 0.5 A g^{-1} over 150 cycles, respectively. The excellent lithium-storage capabilities could be ascribed to the synergistic effect of the nanometer-scale size of the tin chalcogenide particles and the conductivity of carbon. In addition, other series of tin-based composites, that is, Sn/C, SnS_2/C, $SnSe_2$/C, and SnTe/C, were also synthesized in a similar way, demonstrating the general applicability of the one-pot route developed in this work.

ASSOCIATED CONTENT

Supporting Information

The Supporting Information is available free of charge at https://pubs.acs.org/doi/10.1021/acsomega.1c01647.

Figures showing additional characterization data, including SEM, TEM, XPS, XRD, EDX mapping, Raman spectrum, TGA, and Li-storage performances, for tin chalcogenide anodes (PDF)

AUTHOR INFORMATION

Corresponding Author

Miao Wang − *Institute for Advanced Study, Shenzhen University, Shenzhen 518060, China; College of Physics and Optoelectronic Engineering, Shenzhen University, Shenzhen 518060, China*; Email: wm306@szu.edu.cn

Authors

Xianyu Liu − *School of Chemistry and Chemical Engineering, Lanzhou City University, Lanzhou 730070, China*; orcid.org/0000-0003-3087-0368

Tayyaba Najam − *Institute for Advanced Study, Shenzhen University, Shenzhen 518060, China; College of Physics and Optoelectronic Engineering, Shenzhen University, Shenzhen 518060, China*; orcid.org/0000-0002-9284-9401

Ghulam Yasin − *Institute for Advanced Study, Shenzhen University, Shenzhen 518060, China; College of Physics and Optoelectronic Engineering, Shenzhen University, Shenzhen 518060, China*; orcid.org/0000-0001-8794-3965

Mohan Kumar − *Institute for Advanced Study, Shenzhen University, Shenzhen 518060, China; College of Physics and Optoelectronic Engineering, Shenzhen University, Shenzhen 518060, China*

Complete contact information is available at:

https://pubs.acs.org/10.1021/acsomega.1c01647

Notes

The authors declare no competing financial interest.

■ ACKNOWLEDGMENTS

We acknowledge support from the Doctoral Research Fund of Lanzhou City University (LZCU-BS2020-03).

■ REFERENCES

(1) Lee, A.; Vörös, M.; Dose, W. M.; Niklas, J.; Poluektov, O.; Schaller, R. D.; Iddir, H.; Maroni, V. A.; Lee, E.; Ingram, B.; Curtiss, L. A.; Johnson, C. S. Photo-accelerated fast charging of lithium-ion batteries. *Nat. Commun.* **2019**, *10*, No. 4946.

(2) Xu, Q.; Li, J.-Y.; Sun, J.-K.; Yin, Y.-X.; Wan, L.-J.; Guo, Y.-G. Watermelon-inspired Si/C microspheres with hierarchical buffer structures for densely compacted lithium-ion battery anodes. *Adv. Energy Mater.* **2017**, *7*, No. 1601481.

(3) Manthiram, A.; Song, B.; Li, W. A perspective on nickel-rich layered oxide cathodes for lithium-ion batteries. *Energy Storage Mater.* **2017**, *6*, 125−139.

(4) Tarascon, J. M.; Armand, M. Issues and challenges facing rechargeable lithium batteries. *Nature* **2001**, *414*, 359−367.

(5) Wu, Z.-S.; Ren, W.; Wen, L.; Gao, L.; Zhao, J.; Chen, Z.; Zhou, G.; Li, F.; Cheng, H.-M. Graphene anchored with Co_3O_4 nanoparticles as anode of lithium ion batteries with enhanced reversible capacity and cyclic performance. *ACS Nano* **2010**, *4*, 3187−3194.

(6) Han, X.; Qing, G.; Sun, J.; Sun, T. How many lithium ions can be inserted onto fused C_6 aromatic ring systems? *Angew. Chem., Int. Ed.* **2012**, *51*, 5147−5151.

(7) Huo, K.; Wang, L.; Peng, C.; Peng, X.; Li, Y.; Li, Q.; Jin, Z.; Chu, P. K. Crumpled N-doped carbon nanotubes encapsulated with peapod-like Ge nanoparticles for high-rate and long-life Li-ion battery anodes. *J. Mater. Chem. A* **2016**, *4*, 7585−7590.

(8) Liang, X.; Chen, M.; Zhu, H.; Zhu, H.; Cui, X.; Yan, J.; Chen, Q.; Xia, X.; Liu, Q. Unveiling the solid-solution charge storage mechanism in 1T vanadium disulfide nanoarray cathodes. *J. Mater. Chem. A* **2020**, *8*, 9068−9076.

(9) Zhang, K.; Zhang, T.; Liang, J.; Zhu, Y.; Lin, N.; Qian, Y. A potential pyrrhotite (Fe_7S_8) anode material for lithium storage. *RSC Adv.* **2015**, *5*, 14828−14831.

(10) Xue, H.; Yu, D. Y. W.; Qing, J.; Yang, X.; Xu, J.; Li, Z.; Sun, M.; Kang, W.; Tang, Y.; Lee, C.-S. Pyrite FeS_2 microspheres wrapped by reduced graphene oxide as high-performance lithium-ion battery anodes. *J. Mater. Chem. A* **2015**, *3*, 7945−7949.

(11) Grugeon, S.; Laruelle, S.; Herrera-Urbina, R.; Dupont, L.; Poizot, P.; Tarascon, J. M. Particle size effects on the electrochemical performance of copper oxides toward lithium. *J. Electrochem. Soc.* **2001**, *148*, No. A285.

(12) Shembel, E.; Apostolova, R.; Nagirny, V.; Kirsanova, I.; Grebenkin, P.; Lytvyn, P. Electrolytic molybdenum oxides in lithium batteries. *J. Solid State Electrochem.* **2005**, *9*, 96−105.

(13) Lin, Y.-S.; Duh, J.-G.; Hung, M.-H. Shell-by-shell synthesis and applications of carbon-coated SnO_2 hollow nanospheres in lithium-ion battery. *J. Phys. Chem. C* **2010**, *114*, 13136−13141.

(14) Chen, M.; Chao, D.; Liu, J.; Yan, J.; Zhang, B.; Huang, Y.; Lin, J.; Shen, Z. Rapid Pseudocapacitive Sodium-Ion Response Induced by 2D Ultrathin Tin Monoxide Nanoarrays. *Adv. Funct. Mater.* **2017**, *27*, No. 1606232.

(15) Kim, T.-J.; Kim, C.; Son, D.; Choi, M.; Park, B. Novel SnS_2-nanosheet anodes for lithium-ion batteries. *J. Power Sources* **2007**, *167*, 529−535.

(16) Qu, B.; Ma, C.; Ji, G.; Xu, C.; Xu, J.; Meng, Y. S.; Wang, T.; Lee, J. Y. Layered SnS_2-reduced graphene oxide composite - a high-capacity, high-rate, and long-cycle life sodium-ion battery anode material. *Adv. Mater.* **2014**, *26*, 3854−3859.

(17) Ueda, A.; Nagao, M.; Inoue, A.; Hayashi, A.; Seino, Y.; Ota, T.; Tatsumisago, M. Electrochemical performance of all-solid-state lithium batteries with Sn_4P_3 negative electrode. *J. Power Sources* **2013**, *244*, 597−600.

(18) Kim, Y.; Kim, Y.; Choi, A.; Woo, S.; Mok, D.; Choi, N.-S.; Jung, Y. S.; Ryu, J. H.; Oh, S. M.; Lee, K. T. Tin Phosphide as a promising anode material for Na-ion batteries. *Adv. Mater.* **2014**, *26*, 4139−4144.

(19) Park, M.-H.; Kim, K.; Kim, J.; Cho, J. Flexible Dimensional control of high-capacity Li-ion-battery anodes: From 0D hollow to 3D porous germanium nanoparticle assemblies. *Adv. Mater.* **2010**, *22*, 415−418.

(20) Wang, X.-L.; Han, W.-Q.; Chen, H.; Bai, J.; Tyson, T. A.; Yu, X.-Q.; Wang, X.-J.; Yang, X.-Q. Amorphous hierarchical porous GeO_x as high-capacity anodes for Li ion batteries with very long cycling life. *J. Am. Chem. Soc.* **2011**, *133*, 20692−20695.

(21) Jo, G.; Choi, I.; Ahn, H.; Park, M. J. Binder-free Ge nanoparticles-carbon hybrids for anode materials of advanced lithium batteries with high capacity and rate capability. *Chem. Commun.* **2012**, *48*, 3987−3989.

(22) Xue, D.-J.; Xin, S.; Yan, Y.; Jiang, K.-C.; Yin, Y.-X.; Guo, Y.-G.; Wan, L.-J. Improving the electrode performance of Ge through Ge@C core-shell nanoparticles and graphene networks. *J. Am. Chem. Soc.* **2012**, *134*, 2512−2515.

(23) Seng, K. H.; Park, M.-H.; Guo, Z. P.; Liu, H. K.; Cho, J. Self-assembled germanium/carbon nanostructures as high-power anode material for the lithium-ion battery. *Angew. Chem., Int. Ed.* **2012**, *51*, 5657−5661.

(24) Cui, G.; Hu, Y.-S.; Zhi, L.; Wu, D.; Lieberwirth, I.; Maier, J.; Müllen, K. A one-step approach towards carbon-encapsulated hollow tin nanoparticles and their application in lithium batteries. *Small* **2007**, *3*, 2066−2069.

(25) Zhao, Z. W.; Yao, Z. P. G. P.; Liu, H. K. Mesoporous carbon-tin nanocomposites as anode materials for Li-ion battery. *J. Mater. Sci. Technol.* **2008**, *24*, 657−660.

(26) Li, S.; Zheng, J.; Zuo, S.; Wu, Z.; Yan, P.; Pan, F. 2D hybrid anode based on SnS nanosheet bonded with graphene to enhance electrochemical performance for lithium-ion batteries. *RSC Adv.* **2015**, *5*, 46941−46946.

(27) Cai, J.; Li, Z.; Shen, P. K. Porous SnS nanorods/carbon hybrid materials as highly stable and high capacity anode for Li-ion batteries. *ACS Appl. Mater. Interfaces* **2012**, *4*, 4093−4098.

(28) Zhang, Z.; Zhao, X.; Li, J. SnSe/carbon nanocomposite synthesized by high energy ball milling as an anode material for sodium-ion and lithium-ion batteries. *Electrochim. Acta* **2015**, *176*, 1296−1301.

(29) Zhang, L.; Lu, L.; Zhang, D.; Hu, W.; Wang, N.; Xu, B.; Li, Y.; Zeng, H. Dual-buffered SnSe@CNFs as negative electrode with outstanding lithium storage performance. *Electrochim. Acta* **2016**, *209*, 423−429.

(30) Lu, J.; Nan, C.; Li, L.; Peng, Q.; Li, Y. Flexible SnS nanobelts: Facile synthesis, formation mechanism and application in Li-ion batteries. *Nano Res.* **2013**, *6*, 55−64.

(31) Vaughn, D. D.; Hentz, O. D.; Chen, S.; Wang, D.; Schaak, R. E. Formation of SnS nanoflowers for lithium ion batteries. *Chem. Commun.* **2012**, *48*, 5608−5610.

(32) Liu, J.; Gu, M.; Ouyang, L.; Wang, H.; Yang, L.; Zhu, M. Sandwich-like SnS/polypyrrole ultrathin nanosheets as high-performance anode materials for Li-ion batteries. *ACS Appl. Mater. Interfaces* **2016**, *8*, 8502−8510.

(33) Kang, J.-G.; Park, J.-G.; Kim, D.-W. Superior rate capabilities of SnS nanosheet electrodes for Li ion batteries. *Electrochem. Commun.* **2010**, *12*, 307−310.

(34) Tang, Q.; Cui, Y.; Wu, J.; Qu, D.; Baker, A. P.; Ma, Y.; Song, X.; Liu, Y. Ternary tin selenium sulfide ($SnSe_{0.5}S_{0.5}$) nano alloy as the high-performance anode for lithium-ion and sodium-ion batteries. *Nano Energy* **2017**, *41*, 377−386.

(35) Xia, W.; Wang, H.; Zeng, X.; Han, J.; Zhu, J.; Zhou, M.; Wu, S. High-efficiency photocatalytic activity of type II SnO/Sn_3O_4 heterostructures via interfacial charge transfer. *CrystEngComm* **2014**, *16*, 6841−6847.

(36) Kim, Y.; Hwang, H.; Lawler, K.; Martin, S. W.; Cho, J. Electrochemical behavior of Ge and GeX_2 (X = O, S) glasses: Improved reversibility of the reaction of Li with Ge in a sulfide medium. *Electrochim. Acta* **2008**, *53*, 5058−5064.
(37) Wei, Y.; He, J.; Zhang, Q.; Liu, C.; Wang, A.; Li, H.; Zhai, T. Synthesis and investigation of layered GeS as a promising large capacity anode with low voltage and high efficiency in full-cell Li-ion batteries. *Mater. Chem. Front.* **2017**, *1*, 1607−1614.
(38) Liao, H. M.; Sodhi, R. N. S.; Coyle, T. W. Surface composition of AlN powders studied by x-ray photoelectron spectroscopy and bremsstrahlung-excited Auger electron spectroscopy. *J. Vac. Sci. Technol., A* **1993**, *11*, 2681−2686.
(39) Pu, Z.; Wei, S.; Chen, Z.; Mu, S. 3D flexible hydrogen evolution electrodes with Se-promoted molybdenum sulfide nanosheet arrays. *RSC Adv.* **2016**, *6*, 11077−11080.
(40) Xia, J.; Liu, L.; Jamil, S.; Xie, J.; Yan, H.; Yuan, Y.; Zhang, Y.; Nie, S.; Pan, J.; Wang, X.; Cao, G. Free-standing SnS/C nanofiber anodes for ultralong cycle-life lithium-ion batteries and sodium-ion batteries. *Energy Storge Mater.* **2019**, *17*, 1−11.
(41) Wen, Z.; Cui, S.; Kim, H.; Mao, S.; Yu, K.; Lu, G.; Pu, H.; Mao, O.; Chen, J. Binding Sn-based nanoparticles on graphene as the anode of rechargeable lithium-ion batteries. *J. Mater. Chem.* **2012**, *22*, 3300−3306.
(42) Zhang, J.; Cui, R.; Li, X. A.; Liu, X.; Huang, W. A nanohybrid consisting of $NiPS_3$ nanoparticles coupled with defective graphene as a pH-universal electrocatalyst for efficient hydrogen evolution. *J. Mater. Chem. A* **2017**, *5*, 23536−23542.
(43) Wang, Z.; Wang, Z.; Liu, W.; Xiao, W.; Lou, X. W. Amorphous $CoSnO_3$@C nanoboxes with superior lithium storage capability. *Energy Environ. Sci.* **2013**, *6*, 87−91.
(44) Deng, D.; Novoselov, K. S.; Fu, Q.; Zheng, N.; Tian, Z.; Bao, X. Catalysis with two-dimensional materials and their heterostructures. *Nat. Nanotechnol.* **2016**, *11*, 218−230.
(45) Deng, J.; Deng, D.; Bao, X. Robust catalysis on 2D materials encapsulating metals: Concept, application, and perspective. *Adv. Mater.* **2017**, *29*, No. 1606967.
(46) Liu, J.; Wen, Y.; Van Aken, P. A.; Maier, J.; Yu, Y. In situ reduction and coating of SnS_2 nanobelts for free-standing SnS@polypyrrole-nanobelt/carbon-nanotube paper electrodes with superior Li-ion storage. *J. Mater. Chem. A* **2015**, *3*, 5259−5265.
(47) Im, H. S.; Lim, Y. R.; Cho, Y. J.; Park, J.; Cha, E. H.; Kang, H. S. Germanium and tin selenide nanocrystals for high-capacity lithium ion batteries: Comparative phase conversion of germanium and tin. *J. Phys. Chem. C* **2014**, *118*, 21884−21888.
(48) Li, Y.; Tu, J. P.; Huang, X. H.; Wu, H. M.; Yuan, Y. F. Net-like SnS/carbon nanocomposite film anode material for lithium ion batteries. *Electrochem. Commun.* **2007**, *9*, 49−53.
(49) Deng, Z.; Jiang, H.; Hu, Y.; Li, C.; Liu, Y.; Liu, H. Nanospace-confined synthesis of coconut-like SnS/C nanospheres for high-rate and stable lithium-ion batteries. *AIChE J.* **2018**, *64*, 1965−1974.
(50) Zhang, Y.; Su, H.; Wang, C.; Yang, D.; Li, Y.; Zhang, W.; Wang, H.; Zhang, J.; Li, D. Heterostructured SnS/TiO_2@C hollow nanospheres for superior lithium and sodium storage. *Nanoscale* **2019**, *11*, 12846−12852.
(51) Mei, S.; An, W.; Fu, J.; Guo, W.; Feng, X.; Li, X.; Gao, B.; Zhang, X.; Huo, K.; Chu, P. K. Hierarchical micro-flowers self-assembled from SnS monolayers and nitrogen-doped graphene lamellar nanosheets as advanced anode for lithium-ion battery. *Electrochim. Acta* **2020**, *331*, No. 135292.
(52) Zheng, J.; Luo, Y.; Xie, D.; Xiong, X.; Lin, Z.; Wang, G.; Yang, C.; Liu, M. One-pot synthesis of SnS/C nanocomposites on carbon paper as a high-performance free-standing anode for lithium ion batteries. *J. Alloys Compd.* **2019**, *779*, 67−73.
(53) Ma, T.; Sun, L.; Niu, Q.; Xu, Y.; Zhu, K.; Liu, X.; Guo, X.; Zhang, J. N-doped carbon-coated Tin sulfide/graphene nanocomposite for enhanced lithium storage. *Electrochim. Acta* **2019**, *300*, 131−137.
(54) Chen, M.; Zhang, Z.; Si, L.; Wang, R.; Cai, J. Engineering of yolk-double shell cube-like SnS@N-S codoped carbon as a high-performance anode for Li- and Na-ion batteries. *ACS Appl. Mater. Interfaces* **2019**, *11*, 35050−35059.
(55) Li, Y.; Tu, J. P.; Huang, X. H.; Wu, H. M.; Yuan, Y. F. Nanoscale SnS with and without carbon-coatings as an anode material for lithium ion batteries. *Electrochim. Acta* **2006**, *52*, 1383−1389.
(56) Lu, L.; Zhang, L.; Zeng, H.; Xu, B.; Wang, L.; Li, Y. Enhanced cycling performance of Se-doped SnS carbon nanofibers as negative electrode for lithium-ion batteries. *J. Alloys Compd.* **2017**, *695*, 1294−1300.
(57) Zhu, C.; Kopold, P.; Li, W.; Van Aken, P. A.; Maier, J.; Yu, Y. A general strategy to fabricate carbon-coated 3D porous interconnected metal sulfides: Case study of SnS/C nanocomposite for high-performance lithium and sodium ion batteries. *Adv. Sci.* **2015**, *2*, No. 1500200.
(58) Xu, L.; Ma, L.; Zhou, X.; Ling, Y.; Wang, X.; Chen, M. Hierarchical flower-like SnS grafted with glucosamine-derived nitrogen-doped carbon with enhanced reversible Li-storage performance. *Appl. Surf. Sci.* **2018**, *458*, 86−94.
(59) Tao, H.-C.; Yang, X.-L.; Zhang, L.-L.; Ni, S.-B. One-step in situ synthesis of SnS/graphene nanocomposite with enhanced electrochemical performance for lithium ion batteries. *J. Electroanal. Chem.* **2014**, *728*, 134−139.
(60) Lian, Q.; Zhou, G.; Liu, J.; Wu, C.; Wei, W.; Chen, L.; Li, C. Extrinsic pseudocapacitve Li-ion storage of SnS anode via lithiation-induced structural optimization on cycling. *J. Power Sources* **2017**, *366*, 1−8.
(61) Zhao, B.; Wang, Z.; Chen, F.; Yang, Y.; Gao, Y.; Chen, L.; Jiao, Z.; Cheng‡, L.; Jiang, Y. Three-dimensional interconnected spherical graphene framework/SnS nanocomposite for anode material with superior lithium storage performance: Complete reversibility of Li_2S. *ACS Appl. Mater. Interfaces* **2017**, *9*, 1407−1415.
(62) Gurung, A.; Naderi, R.; Vaagensmith, B.; Varnekar, G.; Zhou, Z.; Elbohy, H.; Qiao, Q. Tin selenide - multi-walled carbon nanotubes hybrid anodes for high performance lithium-ion batteries. *Electrochim. Acta* **2016**, *211*, 720−725.
(63) Li, J.; Liu, W.; Chen, C.; Zhao, X.; Qiu, Z.; Xu, H.; Sheng, F.; Hu, Q.; Zheng, Y.; Lin, M.; Pennycook, S. J.; Su, C.; Lu, J. High yield electrochemical exfoliation synthesis of tin selenide quantum dots for high-performance lithium-ion batteries. *J. Mater. Chem. A* **2019**, *7*, 23958−23963.
(64) Xia, J.; Yuan, Y.; Yan, H.; Liu, J.; Zhang, Y.; Liu, L.; Zhang, S.; Li, W.; Yang, X.; Shu, H.; Wang, X.; Cao, G. Electrospun SnSe/C nanofibers as binder-free anode for lithium-ion and sodium-ion batteries. *J. Power Sources* **2020**, *449*, No. 227559.
(65) Tang, Q.; Su, H.; Cui, Y.; Baker, A. P.; Liu, Y.; Lu, J.; Song, X.; Zhang, H.; Wu, J.; Yu, H.; Qu, D. Ternary tin-based chalcogenide nanoplates as a promising anode material for lithium-ion batteries. *J. Power Sources* **2018**, *379*, 182−190.

https://doi.org/10.1021/acsomega.1c01647
ACS Omega 2021, 6, 17391−17399